Unveiling highly-porous nature of a primitive asteroid by thermal imaging

T. Okada[1,2,*], T. Fukuhara[3], S. Tanaka[1,4,5], M. Taguchi[3], T. Arai[6], H. Senshu[7], N. Sakatani[1], Y. Shimaki[1], H. Demura[8], Y. Ogawa[8], K. Suko[8], T. Sekiguchi[9], T. Kouyama[10], J. Takita[11], T. Matsunaga[12], T. Imamura[5], T. Wada[1], S. Hasegawa[1], J. Helbert[13], T. G. Mueller[14], A. Hagermann[15], J. Biele[16], M. Grott[13], M. Hamm[13,28], M. Delbo[17], N. Hirata[8], N. Hirata[18], Y. Yamamoto[1,4], S. Sugita[2], N. Namiki[19,4], K. Kitazato[8], M. Arakawa[18], S. Tachibana[2,1], H. Ikeda[20], M. Ishiguro[21], K. Wada[7], C. Honda[8], R. Honda[22], Y. Ishihara[12], K. Matsumoto[19,4], M. Matsuoka[1], T. Michikami[23], A. Miura[1], T. Morota[2], H. Noda[19], R. Noguchi[1], K. Ogawa[18,24], K. Shirai[1], E. Tatsumi[25,2], H. Yabuta[26], Y. Yokota[1], M. Yamada[7], M. Abe[1,4], M. Hayakawa[1], T. Iwata[1,4], M. Ozaki[1,4], H. Yano[1,4], S. Hosoda[1], O. Mori[1], H. Sawada[1], T. Shimada[1], H. Takeuchi[1,4], R. Tsukizaki[1], A. Fujii[1], C. Hirose[20], S. Kikuchi[1], Y. Mimasu[1], N. Ogawa[1], G. Ono[20], T. Takahashi[1], Y. Takei[1], T. Yamaguchi[1,$], K. Yoshikawa[20], F. Terui[1], T. Saiki[1], S. Nakazawa[1], M. Yoshikawa[1,4], S. Watanabe[27,1], Y. Tsuda[1,4]

[1]*Institute of Space and Astronautical Science (ISAS), Japan Aerospace Exploration Agency (JAXA), Sagamihara, Japan,*
[2]*University of Tokyo, Tokyo, Japan,*
[3]*Rikkyo University, Tokyo, Japan,*
[4]*The Graduate University for Advanced Studies, SOKENDAI, Hayama, Japan.*
[5]*University of Tokyo, Kashiwa, Japan,*
[6]*Ashikaga University, Ashikaga, Japan,*
[7]*Planetary Exploration Research Center, Chiba Institute of Technology, Narashino, Japan,*
[8]*University of Aizu, Aizu-Wakamatsu, Japan,*
[9]*Hokkaido University of Education, Asahikawa, Japan,*
[10]*National Institute of Advanced Industrial Science and Technology (AIST), Tokyo, Japan,*
[11]*Hokkaido Kitami Hokuto High School, Kitami, Japan,*
[12]*National Institute for Environmental Studies (NIES), Tsukuba, Japan,*
[13]*German Aerospace Center (DLR), Berlin, Germany,*
[14]*Max-Planck Institute for Extraterrestrial Physics, Garching, Germany,*
[15]*University of Stirling, Stirling, UK,*
[16]*German Aerospace Center (DLR), Cologne, Germany,*
[17]*Universite Cote d'Azur, Observatoire de la Côte d'Azur, CNRS, Laboratoire Lagrange, Nice, France*
[18] *Kobe University, Kobe, Japan,*
[19]*National Astronomical Observatory of Japan (NAOJ), Mitaka, Japan,*
[20]*Research and Development Directorate, Japan Aerospace Exploration Agency (JAXA), Sagamihara, Japan,*
[21]*Seoul National University, Seoul, South Korea,*
[22]*Kochi University, Kochi, Japan,*
[23]*Kindai University, Higashi-Hiroshima, Japan,*
[24]*Space Exploration Center, Japan Aerospace Exploration Agency (JAXA), Sagamihara, Japan,*
[25]*Instituto de Astrofísica de Canarias, University of La Laguna, La Laguna, Tenerife, Spain*
[26]*Hiroshima University, Higashi-Hiroshima, Japan,*
[27]*Nagoya University, Nagoya, Japan.*
[28]*University of Potsdam, Potsdam, Germany*

*Corresponding author (Email: okada@planeta.sci.isas.jaxa.jp)
$Current affiliation: Mitsubishi Electric Corporation, Kamakura, Kanagawa, Japan.

C-type asteroids[1] are relics of early solar system that preserves primitive materials since they formed ~4.6 Ga. They are likely analogues to carbonaceous chondrites[2,3] and key targets for understanding planetary formation processes. However, their physical properties remain poorly known, since carbonaceous chondrite meteoroids tend not to survive entry to Earth. Here we report the first global one-rotation thermographic images of an asteroid in history, taken by the thermal imager[4] onboard Hayabusa2[5], indicating C-type asteroid 162173 Ryugu has similar temperatures between boulders and their surroundings with the derived thermal inertia of ~300 J m^{-2} $s^{-0.5}$ K^{-1} (tiu, hereafter). Contrary to the predicted surface with regolith and dense boulders, this low thermal inertia suggests the boulders more porous than typical carbonaceous chondrites[6], and the surroundings covered with porous fragments of > 10 cm, which was proven by close-up thermal images. Flat diurnal temperature profiles suggest a strong surface roughness effect[7,8]. We also discovered colder boulders in the close-up thermal images, with the thermal inertia of > 600 tiu, corresponding to dense boulders like typical carbonaceous chondrites[6]. These results constrain the formation history of Ryugu that the asteroid should be a rubble pile formed from impact fragments of a parent body with micro porosity[9] of ~30 to 50 % that experienced a low degree of consolidation, hypothesizing a missing link from fluffy dust to dense celestial bodies[10]. Dense boulders might originate from consolidated innermost region or might be an exogenic origin.

C-type asteroids are the most abundant taxonomic class in the outer main-belt and display reflectance spectra with weak or no features and with flat or very moderate slopes[2,3]. Ground-based and space-based remote observations of Ryugu[11] have characterized the target asteroid's taxonomy as C-type, its rotation period of 7.63 hours, its diameter of ~0.85 km, and its global thermal inertia from 150 to 300 tiu, having been interpreted as a surface covered with millimeter scale granules.

After the spacecraft's arrival at the Home Position (HP), 20 km earthward from Ryugu, Hayabusa2 globally observed the asteroid[12-14], confirming its size, rotation rate and albedo within the predicted ranges, but finding its structure to be double top-shaped, with perpendicularly retrograde rotation[12], and subdued absorptions around 0.7 and 3 μm bands, indicating minerals less hydrated or dehydrated in the past[13,14]. Ryugu has a bulk density[12] of 1190 ± 20 kg m^{-3} and its surface is evenly covered with boulders[13], without the kind of smooth terrains found on 25143 Itokawa[15]. These facts indicate that Ryugu is a rubble-pile asteroid with bulk porosity of 50 % or higher, assuming the asteroid is composed of CI (~2420 kg m^{-3}) or CM (~2960 kg m^{-3}) carbonaceous chondrites[6].

Thermal imaging was conducted to investigate the surface physical state, especially in terms of particle size, porosity, boulder abundance, and surface roughness, derived from the thermal inertia, which is remotely sensed without physical contact - even for porous or loosely-bound surfaces. The surfaces of the Moon, Mars, and large satellites are predominantly covered with regolith that is formed by hypervelocity meteoritic impacts. However, the surface of small bodies remains poorly known[16] since a majority of impact ejecta might escape due to low gravity, depending on the physical properties of the surface materials, so that their surface physical state needs in-depth investigation.

The first set of high-resolved global thermal infrared images of an asteroid in history was obtained on 30 June 2018, with ~18 m/pixel or ~50 pixels across the disk of Ryugu, covering its rotation in steps of 6°. Temperatures of the observed hemisphere ranged from 300 to 370 K for the solar distance of 0.987 au, at the typical solar phase angle of 18.5°, and a rough surface of porous materials was preliminary indicated from the peak temperatures and flat diurnal profiles[7,8].

Higher resolution one-rotation thermal image sets have been taken from 5 km altitude, with spatial resolution of ~4.5 m/pixel at the solar distance of 1.057 au, during the Mid-Altitude Observation Campaign on 1 August 2018. Global thermal images of Ryugu at 90° steps show the brightness temperature distribution on the asteroid (Fig. 1), enhanced from 270 K (black) to 360 K (white). The colder regions such as the shadows are black, while the hottest points on roots of boulders are white, due to self-heating or possible existence of fine-grained sediments. Geologic features are seen including the largest boulder Otohime Saxum (~160 m size) at the south pole, the largest crater Urashima (~270 m diameter), the ridge around the equator, and other boulders, craters, and grabens. Surprisingly the boulders show similar temperatures to the surroundings while, before

arrival, they were expected to be consolidated and observed as cold spots.

A color-scale brightness temperature image of Ryugu plotted on the asteroid shape model (SHAPE_SFM_200k_v20180804) is compared with simulated images[20] for eight uniform thermal inertia models from 50 to 1000 tiu (Fig.2). Although none of them matches to the observations perfectly, the apparent global thermal inertia of Ryugu is most suitable to 300 ± 100 tiu for both of large boulders and the surrounding surfaces. It is also valid for the largest boulder Otohime Saxum whose surface is apparently flat[13].

Diurnal temperature profiles of six different sites on Ryugu are shown in Fig.3, including a large flat boulder at the south pole, a medium sized boulder in the equatorial region, and the surrounding sites at low- and mid-latitudes both at northern and southern hemispheres. These profiles are compared to the calculation[17] for uniform thermal inertias. An extremely high surface roughness[7,8] might explain these flat diurnal profiles, when observed from a relatively small solar phase angle of ~19°. For such a rough surface model, it becomes colder at the nadir point where not only the sunlit hot, but the shadowed cold surfaces are observed, while it becomes hotter at the earlier and later local times where the sunlit surfaces are selectively observed but most of shadowed areas are invisible from the spacecraft. The diurnal temperature profile could be explained with the global surface thermal inertia of 327 ± 127 tiu with a root-mean-square surface roughness of 0.4 ± 0.05[8]. Although a two-layer surface model also explains the shift of peak temperature and delay from the local noon, it never matches the flat diurnal temperature profiles[18]. Similar flat diurnal temperature profiles were observed on the surface of comets[19] 103P/Heartley-2 and 9P/Tempel-1, suggesting these cometary surfaces might be covered with a rough, granular or rugged, probably highly-porous material.

After September 2018, Hayabusa2 started descent operations for sampling touchdowns, as well as for the release of MINERVA-II twin rovers[20] and MASCOT lander[21]. Every time during descent operations, close-up thermal images were taken by TIR down to the altitudes below 60 m for the lander release operations and below 20 m for the samplings and rehearsals. Thermal images of these local sites were taken at a few cm/pixel resolution.

Close-up thermal images were taken during the touchdown rehearsal TD1-R1-A near the sampling site on 15 October 2018 at 1.28 au from the sun, proving the surrounding surface is not covered with soils nor granules but dominantly with boulders (Figs. 4a and 4c). This indicates that the surface features found in the close-up images are evenly distributed around the asteroid, causing similar temperature profiles between large boulders and the surroundings. Most boulders have temperatures typically from 300 to 310 K, corresponding to highly-porous materials with 200 to 300 tiu, as predicted by global thermal images.

We discovered in the close-up images a few boulders below 280 K (Figs. 4b and 4d), corresponding to 600 to 1000 tiu (typical value of carbonaceous chondrites[6]). The surface of Ryugu is dominated by highly-porous boulders, except for some dense boulders similar to carbonaceous chondrite meteorites. This is consistent with the images taken by the camera MASCam[22] on MASCOT showing that a large majority of boulders have cauliflower-like crumbly surfaces, while a minority have flat surfaces.

The average thermal inertia is consistent with that of 282^{+93}_{-35} tiu derived from *in situ* measurements of a single boulder using the radiometer MARA[23] on MASCOT, and consistent with terrestrial and space remote observations[11]. The boulder observed by MARA seems to be typical for boulders distributed globally on Ryugu. Those highly-porous boulders should have micro porosity $\emptyset_\mu$ of 30 to 50 % in vacuum conditions[23-25].

Accounting for the asteroid's bulk density, Ryugu must have a bulk porosity $\emptyset_b$ of 50 to 60 %, assuming it consists of materials of CI or CM chondrites, respectively[12]. The macro porosity $\emptyset_m$ caused by voids between rocks, defined as $\emptyset_m = 1 - (1 - \emptyset_b)/(1 - \emptyset_\mu)$, should be below 20 % for $\emptyset_\mu$ of 50 %, or 30 to 40 % for $\emptyset_\mu$ of 30 %, and Ryugu is a loosely packed rubble pile asteroid made of porous materials formed under microgravity conditions. A trend found for small asteroids having lower thermal inertia compared with typical carbonaceous chondrites[26] might be caused not by fine regolith as predicted but by porous boulders. A similarly low thermal inertia of ~300 tiu was also reported for B-type asteroid 101955 Bennu explored by the OSIRIS-REx mission[27].

160   These facts might constrain the formation history of Ryugu proposed in the previous study[13]. Ryugu could be formed from fragments of a parent body that experienced a low degree of consolidation of originally porous materials. This is the direct evidence of less consolidated nature of C-type asteroids formed from fluffy dust or pebbles in the early solar system. This discovery also implies that those large asteroids in the main belt with high porosity[9] could be formed in the similar
165 way and they are very common among the C-type asteroids. Moreover, those less consolidated materials might have low mechanical strength which cannot survive during atmospheric entry. This might be a reason that the spectra did not match perfectly with the meteorite samples on the Earth[13,14]. Dense boulders might be formed at a consolidated inner core of the parent body, or might be an exogenic origin such as surviving fragments of meteoritic impacts. Highly porous physical
170 state might have been in common with planetesimals that formed from fluffy dust[10] in the early solar system and could have strongly affected planetary formation processes such as cratering and collisional fragmentation by attenuating shock propagation. The possibility still cannot be ruled out that the low thermal inertia and the low density of Ryugu are due to materials different from carbonaceous chondrites such as the organic-rich material discovered on Comet
175 67P/Churymov-Gerasimenko[28]. This question will however be resolved upon sample return.

Online content

Any methods, additional references, Nature Research reporting summaries, source data, statement of data availability and associated accession codes are available at …
180

1.   Rivkin, A. S. et al. Astronomical observations of volatiles on asteroids. in Asteroids IV, eds by Michel, P., DeMeo, F. E., and Bottke, W. F., U. Arizona Press, 65-87 (2015).

2.   Tholen, D. J., Asteroid taxonomic classifications. in *Asteroids II*. Tucson: University of Arizona Press. 1139–1150 (1989).

185 3.   DeMeo, F. E., Alexander, C. M. O., Walsh, K. J., Chapman, C. R., & Binzel, R. P. The compositional structure of the asteroid belt. in Asteroids IV, eds by Michel, P., DeMeo, F. E., and Bottke, W. F., U. Arizona Press, 13–41 (2015).

4.   Okada, T. et al. Thermal Infrared Imaging experiments of C-Type Asteroid 162173 Ryugu on Hayabusa2. *Space Science Reviews* **208**, 255-286 (2017).

190 5.   Tsuda, Y. et al. Flight status of robotic asteroid sample return mission Hayabusa2. *Acta Astronautica* **127**, 702-709 (2016).

6.   Flynn, G.J., Consolmagno, G.J., Brown, P., & Macke, R. J. Physical properties of the stone meteorites: Implications for the properties of their parent bodies. *Chemie der Erde*, 78, 269-298 (2018).

195 7.   Rozitis, B. & Green, S. F. Directional characteristics of thermal-infrared beaming from atmosphereless planetary surfaces – a new thermophysical model. *Mon. Not. R. Astron. Soc.* **415**, 2042-2062 (2011).

8.   Shimaki, Y. et al. Surface roughness and thermal inertia of asteroid Ryugu inferred from TIR on Hayabusa2. *Lunar Planet. Sci. Conf.* **50**, The Woodlands, TX, #1724 (2019).

9.   Britt, D. T., Yeomans, D., Housen, K., & Consolmagno, G. Asteroid density, porosity, and structure, in
200 *Asteroid III*, eds by Bottke, W. F., Jr., Cellino, A., Paolicchi, P., & Binzel R. P., Univ. Arizona Press, Tucson, 485-500 (2002).

10.   Arakawa, S., Tanaka, H., Kataoka, A., & Nakamoto, T. Thermal conductivity of porous aggregates, *Astron. Astrophys.* **608**, L7 (2017).

11.   Mueller, T. G. et al. Hayabusa-2 mission target asteroid 162173 Ryugu (1999 JU3): Searching for the
205 object's spin-axis orientation. *Astron. Astrophys.* **599**, A103 (2017).

12.   Watanabe, S. et al. Hayabusa2 arrives at the carbonaceous asteroid 162173 Ryugu - A spinning top-shaped rubble pile. *Science* **464**, 268-272 (2019).

13.   Sugita, S. et al. The geomorphology, color, and thermal properties of Ryugu: Implications for parent-body processes. *Science* **464**, 552 (2019).

210 14.   Kitazato, K. et al. Surface composition of asteroid 162173 Ryugu as observed by the Hayabusa2 NIRS3 instrument. *Science 464*, 272-275 (2019).

15. Fujiwara, A. et al. The rubble-pile asteroid Itokawa as observed by Hayabusa. *Science* **312**, 1330-1334 (2006).

16. Housen. K. R. & Holsapple, K. A. Ejecta from impact craters. *Icarus* **211**, 856-875 (2011).

215 17. Takita, J., Senshu, H., & Tanaka, S. Feasibility and Accuracy of Thermophysical Estimation of Asteroid 162173 Ryugu (1999 JU3) from the Hayabusa2 Thermal Infrared Imager, *Space Science Reviews* **208**, 287-315 (2017).

18. Biele, J. et al. Effects of dust layers on thermal emission from airless bodies. Prog. Earth Planet. Sci. **6**, 48 (2019).

220 19. Groussin, O. et al. The temperature, thermal inertia, roughness and color of the nuclei of Comets 103P/Hartley 2 and 9P/Tempel 1. *Icarus* **222**, 580–594 (2013).

20. Yoshimitsu, T., Kubota, T., & Tomiki, A. MINERVA-II rovers developed for Hayabusa-2 mission. Abstract, in 11th *Low Cost Planetary Missions Conf.*, June 9-11, 2015, Berlin, Germany.

21. Ho, T.-M. et al. MASCOT - The Mobile Asteroid Surface Scout Onboard the Hayabusa2 Mission. 225 *Space Sci. Rev.* **208**, 339-374 (2017).

22. Jaumann, R. et al. In-situ investigation of asteroid (162173) Ryugu by the Mobile Asteroid Surface Scout (MASCOT) Camera (MASCam). *Science* **365**, 817-820 (2019).

23. Grott, M. et al. Low thermal conductivity boulder with high porosity identified on C-type Asteroid (162173) Ryugu. *Nature Astron.* 3, 971-976 (2019).

230 24. Opeil, C. P., Consolmagno, G. J., Safarik, D. J., & Britt, D. T. Stony meteorite thermal properties and their relationship with meteorite chemical, and physical states. *Met. Plan. Sci.* **47**, 319–329 (2012).

25. Okada, T. Thermal inertia of surface materials of solar system small bodies and its dependence on porosity. *Lunar Planet. Sci. Conf.* **47**, The Woodlands, TX, #1457 (2016).

26. Delbo, M., Mueller, M., Emery, J., Rozitis, B., & Capria, M. T. Asteroid thermophysical modeling, *In* 235 *Asteroid IV*, eds by Michel, P., DeMeo, F. E., & Bottke, W. F. Jr. Univ. Arizona Press, Tucson, 107-128 (2015).

27. DellaGiustina, D. N., Emery, J. P. et al. Properties of rubble-pile asteroid (101955) Bennu from OSIRIS-REx imaging and thermal analysis, *Nature Astron.* **3**, 341-351 (2019).

28. Bardyn, A. et al. Carbon-rich dust in comet 67P/Churyumov-Gerasimenko measured by 240 COSIMA/Rosetta, *Mon. Not. R. Astron. Soc.* **469,** S712–S722 (2017).

250 **Reviewer Information** *Nature* thanks Clark Chapman and the other anonymous reviewer(s) for their contribution to the peer review of this work.

Authors Contributions T.O. led TIR development and experiments, including interpretations of TIR data; TIR development and calibrations: T.O., T.F., S.Tn., M.T., T.A., H.Se., N.S., H.D., Y.O., T.Se., T.K., J.T., 255 T.M., T.Im., T.W., S.Ha., J.H., T.G.M., and A.H.; TIR data acquisitions and reductions; T.O., S.Tn., T.A., H.Se., N.S., Y.S., H.D., Y.O., K.Su., and T.K.; Thermophysical modeling and discussions: T.O., S.Tn., T.A., H.Se., N.S., Y.S., M.DB., J.B., M.G., and M.H.; Shape modeling contributions: Nr.H., Ny.H., Y.Ya., K.M, and A.M..; Landing site selection discussions: K.W., C.Ho., R.H., Y.I., K.M., M.M., T.M., A.M., T.M., H.N., R.N., K.O., K.Sh., E.T., H.Yb., Y.Yo., H.Yn., and M.Ya.; Science operations of spacecraft: M.Ab., M.Hy., T.Iw. 260 M.O., H.Yn., S.Ho., O.M., H.Sw., T.Sh., H.T., R.T., A.F., C.Hi., S.K., Y.M., N.O., G.O., T.T., Y.Ta., T.Y., K.Y., F.T., T.Sa., S.N., M.Yo., S.W., and Y.Ts.; Project administration: S.S,, N.N., K.K., T.O., M.Ar., S.Tc., H.I., M.I., S.Tn., F.T., T.Sa., S.N., M.Yo., S.W., and Y.Ts., Interpretation and writing contribution: T.O., S.Tn., T.A., H.Se., N.S., Y.S., H.D., J.H., J.B., M.G., M.DB., T.G.M., A.H., E.T., T.M., and S.S. All authors discussed the results and commented on the manuscript.
265

Competing conflicts. The authors declare no conflicts of interest associated with this manuscript.

Additional information
Extended data is available for this paper at …
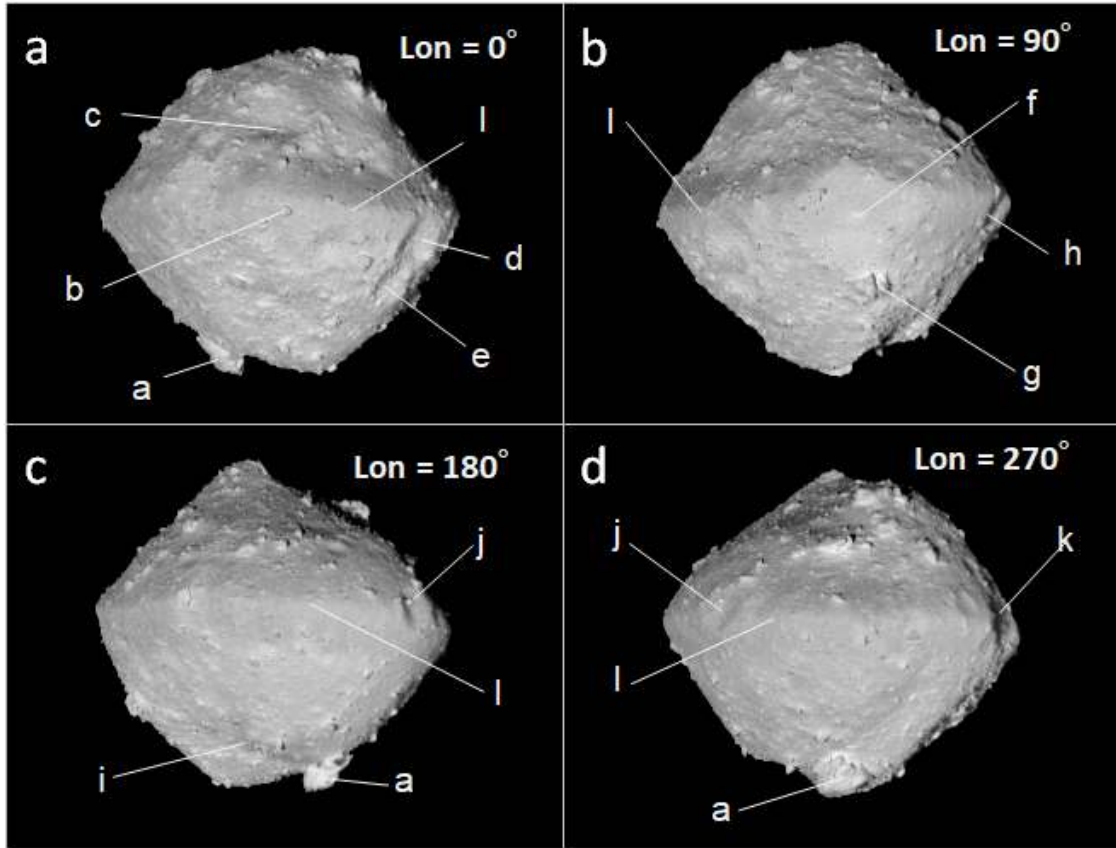**Supplementary information is available for this paper at …**
Reprints and permission information is available at …
**Correspondence and requests for materials** should be addressed to T.O.
Publisher's note: Springer Nature remains neutral with regard to jurisdictional claims in published maps and institutional affiliations.

280

Fig. 1 | Thermal images of Ryugu taken at 5 km altitude during the Mid-Altitude Observation Campaign. a-d, Thermal images were taken on 1 August 2018, at the solar distance of 1.06 au and the SPE angle of 19.0°, **a,** for the local time of 0°, **b,** for the local time of 90°, **c,** for the local time of 180°, and **d,** for the local time of 270°. Relatively higher temperatures in the southern hemisphere were due to the summer season. Geologic features are clearly identified such as (a) Otohime Saxum (the largest boulder near the south pole, 160 m width), (b) Catafo Saxum, (c) Cendrillon crater, (d) Momotaro crater, (e), Kibidango crater, (f) Urashima crater (the largest crater, 270 m diameter), (g) Ejima Saxum, (h) Kintaro crater, (i) Tokoyo Fossa, (j) Brabo crater, (k) Kolobok crater, and (l) Ryujin Dorsum (the equatorial ridge).

290
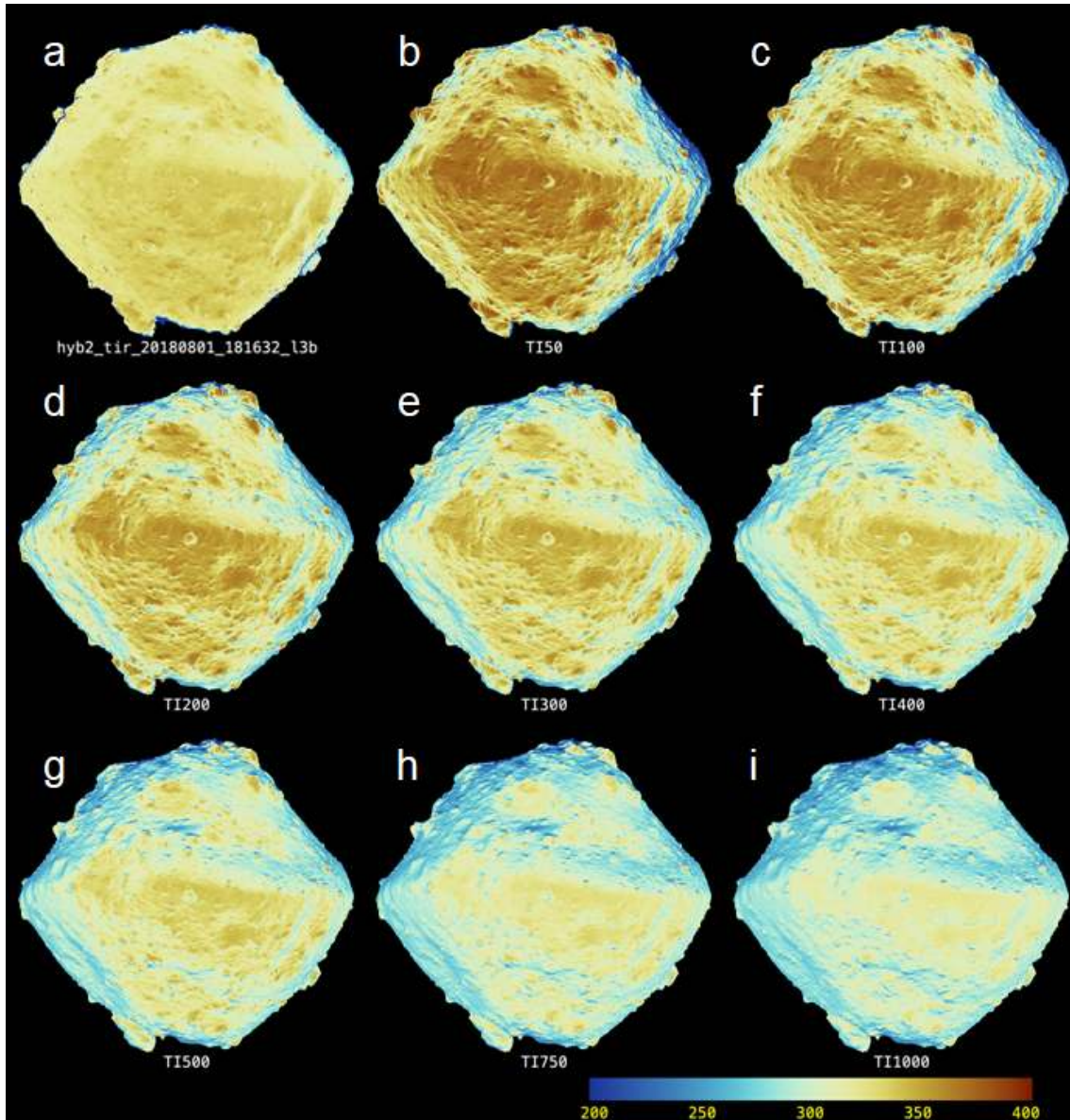
Fig. 2 | Comparison of a temperature plot on the 3D shape model with calculated images for thermal inertias from 50 to 1000 tiu. **a,** A temperature plot in K on the asteroid Ryugu shape model (SHAPE_SFM_200k_v20180804), using the thermal image taken by TIR at 18:16:32 UTC on 1 Aug 2018 during the Mid-Altitude Observation Campaign. **b-i,** Calculated thermal images to be compared with the observation, **b,** assuming the uniform thermal inertia (TI) of 50 tiu, **c,** TI of 100 tiu, **d,** TI of 200 tiu, **e,** TI of 300 tiu, **f,** TI of 400 tiu, **g,** TI of 500 tiu, **h,** TI of 750 tiu, and **i,** TI of 1000 tiu. TI of 300 ± 100 tiu is most suitable to the observation.

	Polygon ID	Longitude	Latitude	Remarks
b	157464	27.8 °E	32.5 °N	Smooth region in northern mid latitude
c	152944	13.9 °E	3.9 °N	Smooth region in northern low latitude
d	147342	0.2 °E	5.5 °S	Catafo Saxum (boulder, PM landmark)
e	147896	2.7 °E	18.3 °S	Smooth region in southern mid latitude
f	194355	329.1 °E	47.0 °S	Smooth region in southern low latitude
g	183108	290.4 °E	68.8 °S	Otohime Saxum (boulder)
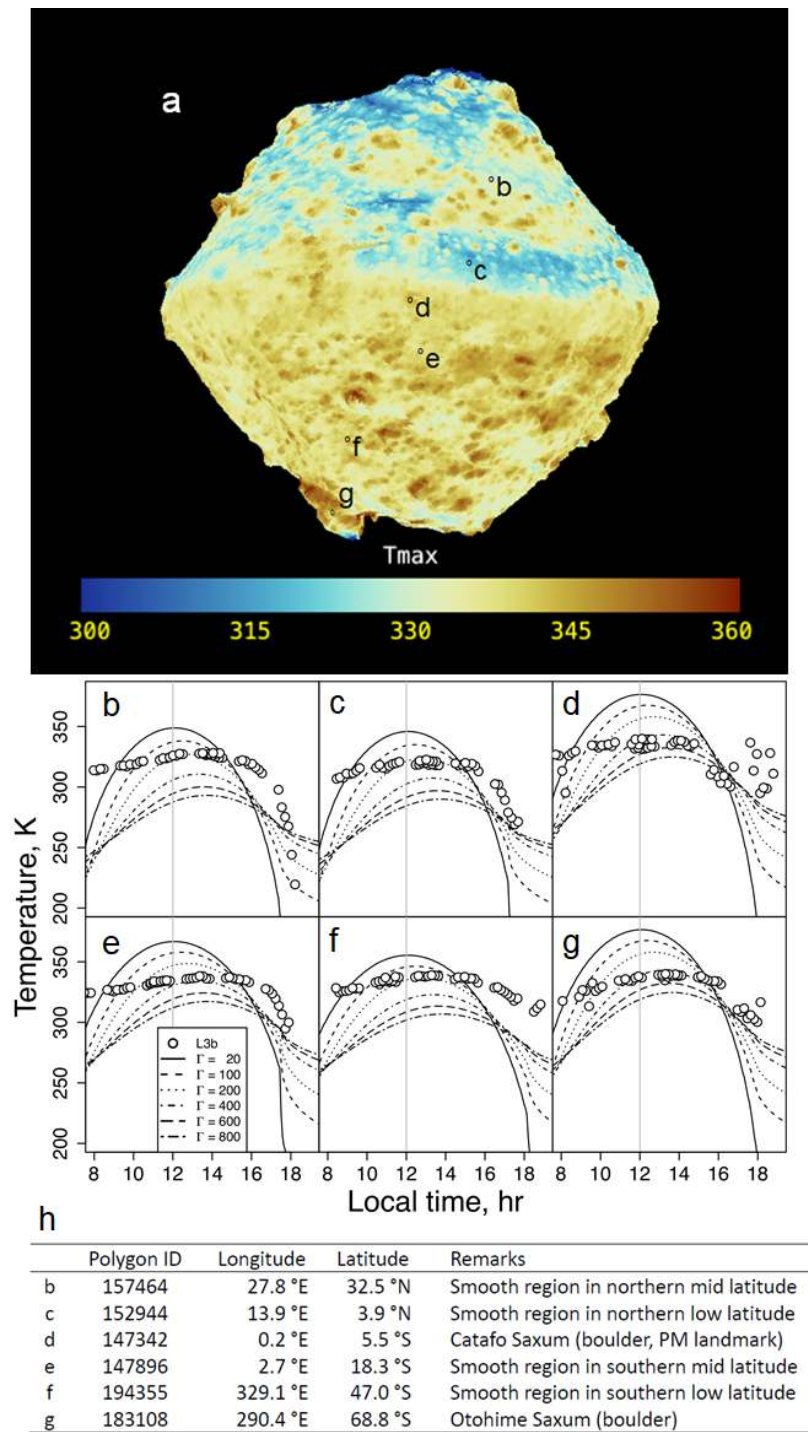
Fig. 3 | Maximum temperature distribution in during one rotation and the diurnal temperature profiles on Ryugu. a, Distribution of maximum temperature in K during one rotation on 1 August 2018 plotted on the Ryugu shape model (SHAPE_SFM_200k_v20180804). **b-g,** Temperature profiles by TIR observation (circles) and by thermal calculation (lines or dotted lines) with uniform thermal inertias from 20 to 800 tiu. **h,** The polygon IDs, the positions in longitude and latitude, and the information of each site of b to g are shown in the table above. The numbers of the color bar are in tiu.

315
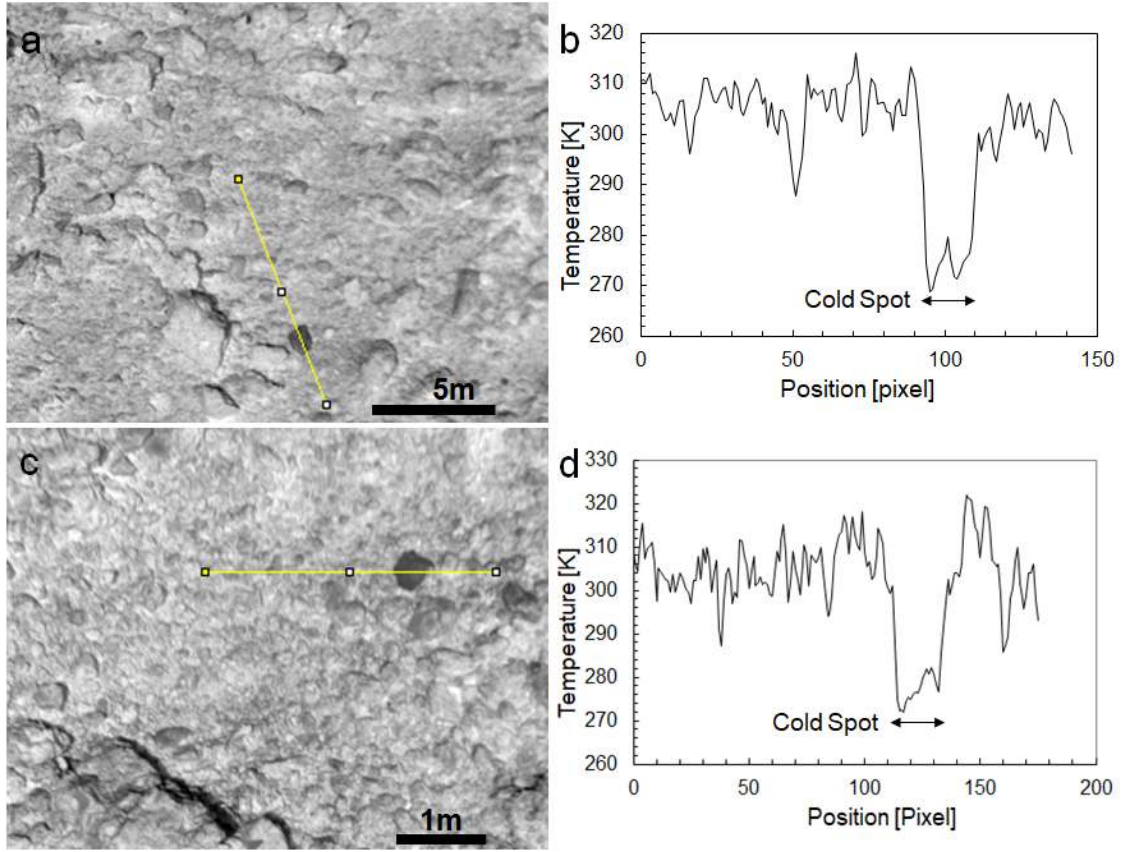
Figure 4 | Cold spots discovered in the close-up thermal images. a, A close-up thermal image taken during the TD1-R1-A Campaign on 15 October 2018, at the solar distance of 1.28 au and the SPE angle of 10.6°, at 13:34:44 UTC from the altitude of 78.8 m. **b,** The temperature profile on the yellow line in the image (a), showing the "cold spot" boulder is identified. **c,** A close-up thermal

320   image at 13:44:20 UTC at the altitude of 21.9 m. **d,** The temperature profile on the yellow line in the image (c), showing the "cold spot" boulder is identified. The surface is basically covered with boulders, and most of them have similar temperatures. The "cold spot" boulders show colder temperatures by more than 20 K, indicating dense and consolidated boulders with higher thermal inertia.

325

METHODS

Hayabusa2 mission and its proximity observation phases. Hayabusa2[5] is the second asteroid sample return mission organized by Japan Aerospace Exploration Agency. The spacecraft is technically inherited from the Hayabusa mission[29], which explored the S-type asteroid 25143 Itokawa[15]. Hayabusa2 was launched by the H-IIA launch vehicle on 3 December 2014, thrusted with ion engine system and with the assist of the Earth's gravity on 3 December 2015, the spacecraft arrived at the target asteroid 162173 Ryugu on 27 June 2018. During a 1.5-years long proximity phase, TIR observes the asteroid for almost two weeks' interval as a nominal plan from the stational position called Home Position (HP), 20 km earthward from the asteroid surface. Specific operations including the descent operations have been conducted and planned. Major operations for the TIR described in this paper are tabulated in Extended Data Table 1.

Asteroid reference model before arrival. Before the launch, the asteroid was illustrated by an artist (Mr. A. Ikeshita) as shown in Extended Data Fig. 1, where the surface was covered with regolith dominated by sands and gravels formed by impact ejecta, and the surface was not dominated by huge boulders but by aqueously altered surfaces with impact craters, according to the information from scientists. Hayabusa2 team constructed the Ryugu reference model called "Ryugoid" for performing the exercise of landing site selection process. An example of the thermal image of Ryugoid is shown in Extended Data Fig. 2, where boulders were identified as "cold spots", assuming the thermal inertia of dense boulders of 1600 tiu, and the granular surroundings of 300 tiu as indicated by averaged thermal inertia by ground observations[11]. Thermal inertia, denoted as $(\rho \kappa c_p)^{0.5}$ expresses surface's thermophysical properties, where ρ is a bulk density, κ is a thermal conductivity, and c_p is a specific heat capacity.

TIR instrument and temperature control. Thermal radiometry has been among the commonly used methods[30-34] in planetary missions to investigate the physical state of planetary surfaces and often conducted along the track of an orbiting spacecraft. In Hayabusa2 mission, however, a two-dimensional imager is requested because the spacecraft stays at a distant stational position due to the low gravity of the small body.

TIR is a thermal imager based on a two-dimensional microbolometer array of 344 x 260 pixels (328 x 248 effective pixels). TIR observes the wavelength range of 8 to 12 μm, from the field of view (FOV) of 16.7° by 12.7°, corresponding to the spatial resolution of 0.88 mrad per pixel. Its design is the same as the Longwave Infrared Camera (LIR)[35] on the Akatsuki Venus Climate Orbiter except for the thermal design. TIR consists of the sensor and data handling unit (TIR-S) and the power supply unit (TIR-AE), mounted on the inside of the +Y panel, as well as the corn-shaped sunshade, mounted on the outside of the -Z panel. Its data processing such as the integration of multiple images, the dark-frame subtraction, and the data compression is conducted in the Digital Electronics (DE). The optics of TIR-S is made of Germanium lens, pointed to the -Z direction, the same as the other optical instruments. TIR-S is mounted on a dedicated panel that is thermally isolated to the surrounding environment, and whose temperature is controlled within a narrow range by the spacecraft heater control electronics (HCE). Hence, the temperature of TIR-S is kept stable even during the descent operations. The detector temperature is controlled with a Peltier thermoelectric device at 313 K (40 °C) within 0.019 K (equivalent to a least significant bit of digital data). Temperatures are accurately monitored within 0.002 K at the sensor package T_{pkg}, the case (the adaptor of 8-12 μm filter) T_{case}, the shutter T_{sht}, and the lens cover T_{lens}. The package, case, and lens temperatures are kept stable within ±0.1 K even during the descent operations, while the shutter temperature increases by 1 K at the lowest altitude where the input of thermal radiation from the asteroid is maximal to warm the shutter. The influence is limited and basically compensated because all the thermal images of TIR is processed after subtraction of the shutter-close dark-frame image from the shutter-open image.

TIR calibration. Pre-flight calibration of TIR has been carried out using three types of calibration targets; a collimator, a cavity blackbody source, and blackbody plates. We used the same apparatus prepared for the calibration of the Longwave Infrared Camera (LIR) onboard Japanese Venus explorer Akatsuki[36]. It allows us to control the temperature of a blackbody plate from -40 to +50 °C in a vacuum chamber. Temperatures of asteroid surface in the daytime are estimated up to 100 °C.

Therefore, we set up another experimental apparatus using an oil bath to control the temperature of the blackbody plate from +50 to +125 °C. These apparatuses enable us to investigate the response of all the pixels of TIR. The measured emissivity of the blackbody plates is 0.925.

The temperature inside of the instrument affects the output of TIR. During the calibration test, we corrected data with the four monitoring temperatures. We found that the shutter temperature is especially effective. Linear relations are seen for each temperature of the calibration target. We found that the better linear relationship appears after package and case temperature correction below;

$$D' = D - 6.125 \ (T_{case} - T_{pkg}), \qquad (1)$$

where D and D' is original and calibrated digital number for each pixel. This calibration corresponds to temperature correction of the gain of A/D converter. After the case and package temperature correction, we carried out shutter temperature correction using the following equation,

$$D'' = D' - 6.158(T_0 - T_{sht}), \qquad (2)$$

where D'' is the calibrated digital number, T_{sht} is shutter temperature, $T_0 = 28$ °C is the standard temperature, following the method in the previous study[41].

After the calibration using the instrument temperatures, we made a look-up table to convert the digital number to the radiance of the target. The blackbody temperature is converted to effective radiance, based on the method[37],

$$I(T) = \int_0^\infty \varepsilon \, B(\lambda, T) R(\lambda) d\lambda, \qquad (3)$$

where ε is the emissivity (equals to 0.925 for the black body plate), λ is wavelength, $R(\lambda)$ is the response function of TIR[4], and $B(\lambda, T)$ is the spectral radiance given by the Planck function. By linear least-squared fitting of output digital number and radiance, we defined the slope $a_{i,j}$ and intercept $b_{i,j}$ for all pixel (i, j) as,

$$D''_{i,j} = a_{i,j} I(T) + b_{i,j}. \qquad (4)$$

A critical problem of the accurate calibration for infrared imagers and thermometers is Size-of-Source Effect[38] (SSE, hereafter). SSE occurs due to scattering and diffraction of thermal radiation within the optical component. We evaluate SSE of TIR using a collimator and a cavity blackbody, whose temperatures were controlled from +20 to +125 °C. The measurements of these targets were carried out in the atmosphere due to the constraints of the apparatus. We found SSE for TIR during the calibration (see Extended Data Fig. 3); the output values become relatively low for the small image of the different calibration targets (collimator < cavity blackbody < blackbody plate). The position of the targets in the image was changed to check the SSE on the sensitivity of each pixels.

For the correction of SSE, we focus on effective diameter of targets, which is defined as $D = 2\sqrt{N/\pi}$ where N is pixel number of the observed target. The effective diameters of collimator and cavity blackbody are about 60 and 125, respectively. And, effective diameters of asteroid Ryugu are around 55 and 180 for Box-A and Mid-altitude observations, respectively. A close-up image where TIR image is fully covered with asteroid surface and a calibration data of blackbody plate have the effective diameter values of D = 322. The SSE was found for continuous observations during a descent operation for gravity measurement on 6 to 7 August 2018. Averaged DN values of Ryugu increased linearly with increasing the effective diameter, but a rapid jump of DN value occurred with an effective diameter larger than 300. The look-up table (LUT, hereafter) applied to the asteroid image is built based on the effective diameter of imaged Ryugu. In the range of $D \leq 300$, LUT is created by linear interpolation and extrapolation of the LUTs for collimator and cavity blackbody. Note that the data for blackbody plate is not fitted to this linear extrapolation due to this higher effective diameter regime ($300 < D \leq 322$). Therefore, we used another linear function derived from the LUT data for blackbody plate and extrapolated values at D = 300 from

lower effective diameter regime (see Extended Data Fig. 4). Using the LUT derived from the effective diameter of the asteroid, the DN values are converted to the radiance values for each pixel using Eq. (4). The derived radiant flux images are converted to brightness temperature images from Eq. (3), assuming the emissivity of 1 independent of the wavelength.

440 **A History of Ryugu formation.** The history of Ryugu formation in the previous study[13], mainly using the results by the optical navigation camera (ONC), proposed three scenarios with the different types of parent bodies before catastrophic disruption; Scenario 1: an aqueously altered parent body dehydrated by internal heating, Scenario 2: an aqueously altered parent body dehydrated by impact heating, and Scenario 3: an incipiently altered parent body. Results of TIR observations might 445 constrain or update the possible scenario of Ryugu formation, suggesting that the Scenario 3 seems to be most suitable as shown below, although further in-depth study including the analysis of returned samples is needed for the final answer.

A scenario is shown mainly using the results of TIR (Extended Data Fig. 5) : (1) Fluffy dust particles containing minerals, water and organics were accumulated to form planetesimals in the 450 early solar system. (2) Planetesimals were kept porous due to a low degree of consolidation under a low gravity condition, even if they might have experienced impact compaction, fragmentation and re-accretion processes. (3) The parent body of Ryugu was kept porous for most of its volume, but its innermost interior might be more consolidated and thermally altered to form a dense core consisted of typical carbonaceous meteorites, if the lithostatic pressure reached the level of its bulk modulus of 455 50 MPa or higher. A gradual increase of degree of consolidation might be expected rather than a clear boundary of the possible inner core. C-type asteroid 253 Mathilde[39] which has a very low spin rate, a low density of 1300 ± 300 kg m^{-3}, and a number of extremely large craters of almost half size of its diameter, may be an example of a porous, loosely-bound rubble-pile asteroid. (4) Intense impact fragmentation by catastrophic disruption occurred to expose the interior materials. (5) Part of 460 impact fragments accreted to form Ryugu. Most of its surface is consisted of porous materials that have undergone only a low degree of consolidation, including large boulders. Some dense boulders might be from the innermost part of the parent body. Alternative scenario might be that a dense small asteroid impacted the porous parent body to form Ryugu by re-accretion of fragments, where the dense rocks might be from the dense impactor. (6) A rubble-pile asteroid that formed from 465 mostly porous fragments has been reshaped to be a double top-shaped[12] due to spin rate change by the Yarkovsky-O'Keefe-Radzievskii-Paddack (YORP) effect[40] and resurfaced by impact cratering and boulder movement.

Code availability. The basic code of the asteroid thermal model that supports the calculation of thermal images with several thermal inertias has been constructed by the previous study[17], which is 470 applicable to any asteroid shape model of even more than one million nodes and capable of calculation of self-heating effect between the nodes facing each other and shadowing effect of insolation by geological features. This code is accessible from the corresponding author upon reasonable request.

475 ## Data availability

TIR global thermal infrared images used for Figs.1a-d are hyb2_tir_20180801_142608_l2.fit for Fig. 1a, hyb2_tir_20180801_162120_l2.fit for Fig. 1b, hyb2_tir_20180801_181632_l2.fit for Fig. 1c, and hyb2_tir_20180801_201144_l2.fit for Fig.1d.

TIR close-up thermal images used for Figs.4a-b are hyb2_tir_20181015_133444_l2.fit, and 480 hyb2_tir_20181015_134420_l2.fit, respectively.

A TIR radiance image plotted on the Ryugu shape model (SHAPE_SFM_200k_v20180804) are used in Fig. 2 as hyb2_tir_20180801_181632_l3b.txt. The data used in this manuscript including the global and close-up thermal images and the calculated thermal images for several thermal inertias, and the plots of diurnal temperature change are available from the corresponding author 485 upon reasonable request. The raw data (L1) and the temperature converted data (L2) of TIR and the corresponding ancillary data for the SPICE tool will be archived in the DARTS data base (darts.isas.jaxa.jp/planet/project/hayabusa2/) by the end of 2019, and will be archived in the PDS4 within one year after the end of its nominal mission, according to the Hayabusa2 science data policy.

490

29. Kawaguchi, J, Uesugi K, & Fujiwara A. The MUSES-C mission for the sample and return—its technology development status and readiness. *Acta. Astronaut.* **5**, 117–123 (2003).

30. Kieffer, H.H., Chase, S., Minor, E., Muench, G. & Neugebauer, G. Preliminary report on infrared radiometric measurements from the Mariner 9 spacecraft. *J. Geophys. Res.* **78**, 4291-4312 (1973).

495
31. Chase, S.C. et al. Mariner 10 infrared radiometer results: Temperatures and thermal properties of the surface of Mercury. *Icarus* **28**, 565-578 (1976).

32. Kieffer, H.H., T. Martin, A. Peterfreund, B. Jakosky, Thermal and albedo mapping of Mars during Viking primary mission. *J. Geophys. Res.* **82**, 4249-4291 (1977).

33. Christensen, P. R.et al. Mars Global Surveyor Thermal Emission Spectrometer experiment:
500   Investigation description and surface science results. *J. Geophys. Res.* **106**, 23,823-23,871 (2001).

34. Paige, D. A. et al. The Lunar Reconnaissance Orbiter Diviner lunar radiometer experiment. *Space Sci. Rev.* **150**, 125-160 (2010).

35. Fukuhara, T. et al. LIR: longwave infrared camera onboard the Venus orbiter Akatsuki. *Earth Planets Space* **63**, 1009–1018 (2011).

505
36. Fukuhara, T. et al. Absolute calibration of brightness temperature of the Venus disk observed by the Longwave Infrared Camera onboard Akatsuki. *Earth, Planets, Space*. **69**, 141, 2017.

37. Arai, T. et al. Thermal Imaging Performance of TIR Onboard the Hayabusa2 Spacecraft. *Space Science Reviews* 208, 239-254, 2017. DOI:10.1007/s11214-017-0353-9.

38. Sanders, P. Dealing with the size-of-source effect in the calibration of direct-reading radiation
510   thermometer, *AIP Conference Proceedings* **1552**, 619-624 (2013).

39. Veverka, J. et al. NEAR Encounter with Asteroid 253 Mathilde: Overview. *Icarus* **140**, 3-16 (1999).

40. Rubincam, D. Radiative spin-up and spin-down of small asteroids. *Icarus* **148**, 2–11 (2000).

14

515

Extended Data Table 1 | TIR major operations around Ryugu before mid-October 2018.

	Date	Solar distance [au]	SPE angle [deg]	Lowest Altitude	Maximum Resolution [/pixel]	Contents of TIR Observations
1	2018/06/06	0.964	16.7	2000 km	Point source	Light curve observations & search for moons
2	2018/06/18	0.971	17.7	200 km	180 m	Light curve observations & search for moons
3	2018/06/30	0.986	18.5	20 km	18 m	Light curve observations & search for moons // First set of HR global thermal images of an asteroid
4	2018/07/10	1.004	19.0	20 km	18 m	Global mapping for 1 rotation : Box-A
5	2018/07/20	1.027	19.2	6.5 km	6 m	Global mapping for 1 rotation : Box-C
6	2018/08/01	1.056	19.0	5 km	4.5 m	Global mapping for 1 rotation : Mid-Altitude
7	2018/08/06-07	1.073	18.7	< 1 km	0.9 m	HR images : Gravity Measurement
8	2018/08/25	1.127	17.5	22 km	20 m	Global mapping for 1 rotation : Box-B (South pole)
9	2018/08/31	1.145	16.9	22 km	20 m	Global mapping for 1 rotation : Box-B (Dusk side)
10	2018/09/20-21	1.209	14.4	50 m	4.5 cm	Close-up images: MINERVA-II release
11	2018/10/03-04	1.244	12.6	50 m 2~3 km	4.5 cm 1.8 m	Close-up images: MASCOT release HR images : MASCOT hovering at 3 km
12	2018/10/14-15	1.273	10.8	10 m	0.9 cm	Close-up images: TD1-R1-A

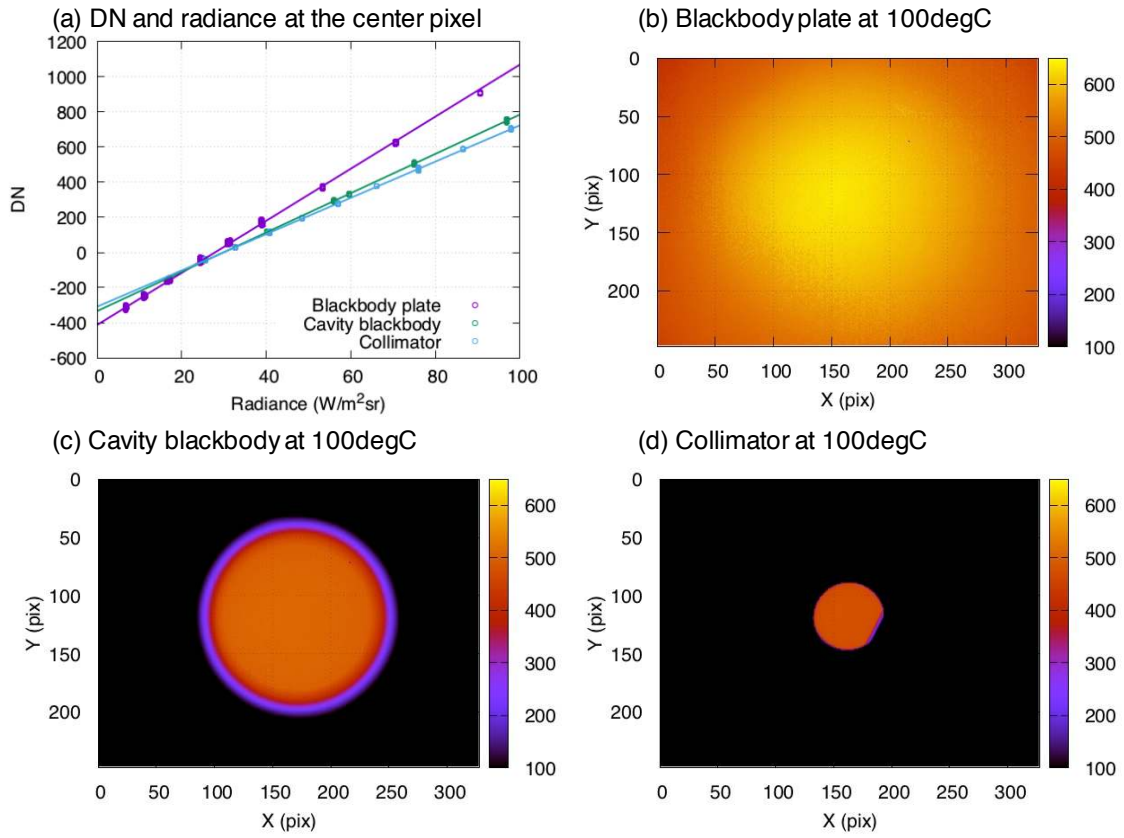SPE, Sun-Probe-Earth   HR, high-resolution,

520

Extended Data Fig.1 | An expected appearance of asteroid Ryugu before arrival. An artist's illustration of asteroid 162173 Ryugu before launch, which was not dominated by huge boulders but aqueously altered surface with impact craters (by A. Ikeshita).
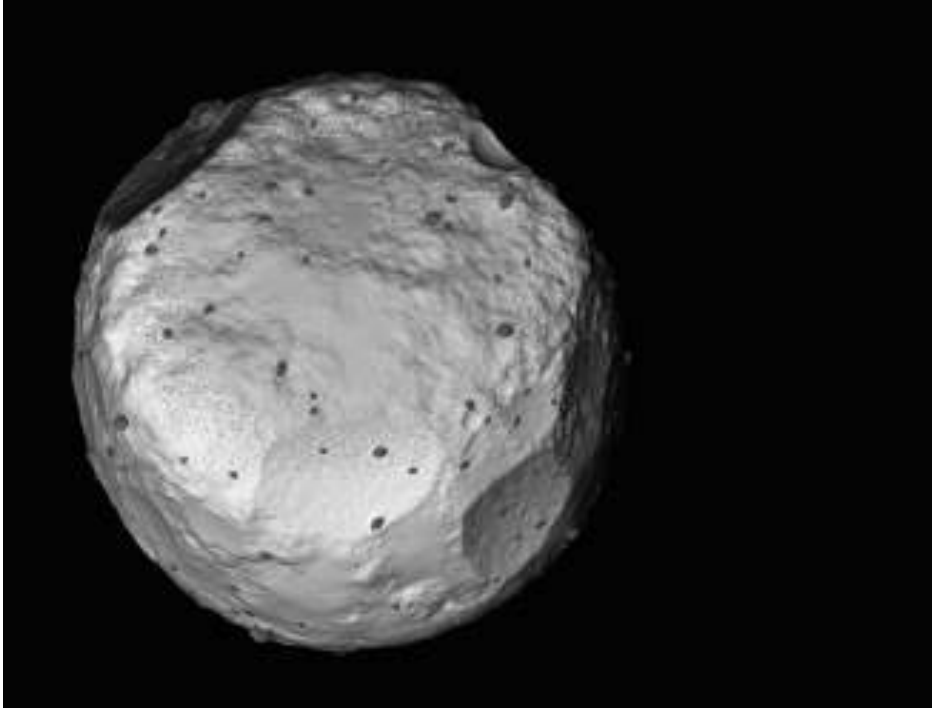
**Extended Data Fig.2 | An expected thermal image of asteroid Ryugu before arrival.** A thermal image of the reference model "Ryugoid" shows the surface covered with regolith and some boulders, and most of boulders are identified as "cold spots".

530

(a) DN and radiance at the center pixel

(b) Blackbody plate at 100degC

(c) Cavity blackbody at 100degC

(d) Collimator at 100degC

535

Extended Data Fig. 3 | Temperature calibration of TIR using multiple apparatuses. a, An
example of TIR pixel response of a center pixel (164, 124) obtained by the ground-based calibration.
The black dots and line show the data for blackbody plates and those linear regression. The purple
and green dots show the data for cavity blackbody and collimator, respectively. **b-d,** Thermal images
540   of TIR using the different apparatuses: **b,** the blackbody plate, **c,** the cavity blackbody, and **d,** the
collimator.

(a) Slope value
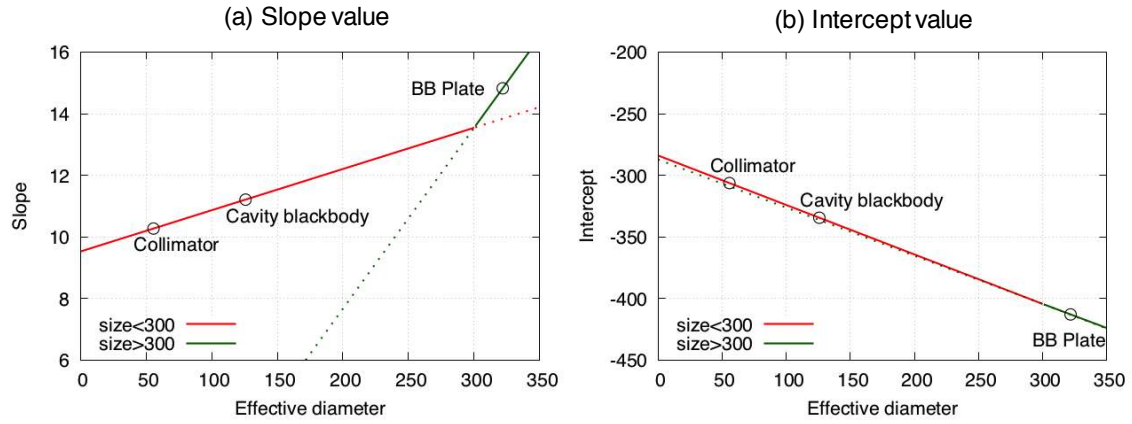
(b) Intercept value

Extended Data Fig. 4 | Effective diameter dependence of the LUT for TIR calibration. This figures show the values of slope a and intercept b at the center pixel of (164, 124) in terms of the effective diameter D of the target. If $D \leq 300$, the red lines are applied derived from the data for the collimator and the cavity blackbody source. If $300 < D \leq 322$, the green lines are applied.

550
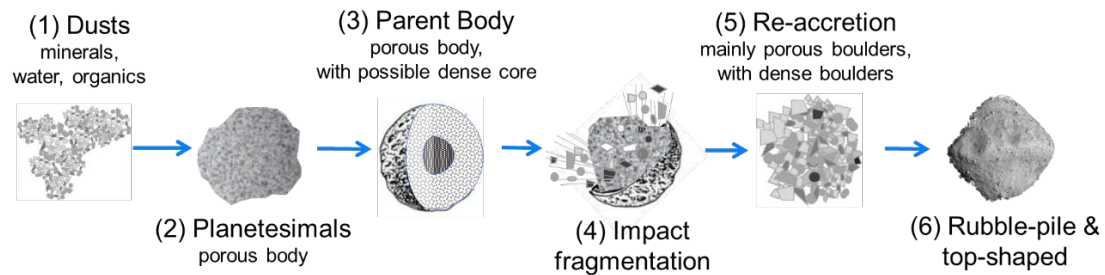
Extended Data Fig. 5 | A formation scenario of Ryugu from a porous parent body. (1) The formation started with fluffy dust in the solar nebula. (2) Porous planetesimals were formed by accretion of dust or pebbles. (3) The parent body of Ryugu might remain porous due to a low degree of consolidation. A clear boundary of the inner core is illustrated but a gradual increase of consolidation by depth could be expected. (4) Impact fragmentation of the parent body occurred. Some large fragments are the boulders on Ryugu. (5) Part of fragments were re-accreted to form Ryugu with porous boulders and sediments on the surface, with some dense boulders originated form the inner core. (6) Re-shape by rotation rate change to form a double top-shape.